# Superharmonic Imaging with Chirp Coded Excitation: Filtering Spectrally Overlapped Harmonics

Sevan Harput, *Member, IEEE*, James McLaughlan, *Member, IEEE*, David M. J. Cowell, *Member, IEEE*, and Steven Freear, *Senior Member, IEEE*

***Abstract*—Superharmonic imaging improves the spatial resolution by using the higher-order harmonics generated in tissue. The superharmonic component is formed by combining the third, fourth and fifth harmonics, which has low energy content and therefore poor SNR. This study uses coded excitation to increase the excitation energy. The SNR improvement is achieved on the receiver side by performing pulse compression with harmonic matched filters.**

**The use of coded signals also introduces new filtering capabilities that are not possible with pulsed excitation. This is especially important when using wideband signals. For narrowband signals the spectral boundaries of the harmonics are clearly separated and thus easy to filter, however the available imaging bandwidth is underused. Wideband excitation is preferable for harmonic imaging applications to preserve axial resolution, but it generates spectrally overlapping harmonics that are not possible to filter in time and frequency domains. After pulse compression this overlap increases the range sidelobes, which appear as imaging artifacts and reduce the B-mode image quality. In this study, the isolation of higher-order harmonics was achieved in another domain by using the Fan Chirp Transform (FChT).**

**To show the effect of excitation bandwidth in superharmonic imaging, measurements were performed by using linear frequency modulated chirp excitation with varying bandwidths of $10-50\%$. Superharmonic imaging was performed on a wire phantom using a wideband chirp excitation. Results were presented with and without applying the FChT filtering technique by comparing the spatial resolution and sidelobe levels. Wideband excitation signals achieved a better resolution as expected, however range sidelobes as high as $-23$ dB were observed for the superharmonic component of chirp excitation with $50\%$ fractional bandwidth. The proposed filtering technique achieved $>50$ dB range sidelobe suppression and improved the image quality without affecting the axial resolution.**

***Index Terms*—Superharmonic imaging, Fan Chirp transform, sidelobe suppression, spectral overlap, chirp coded excitation.**

## I. Introduction

In medical ultrasound imaging, the spatial resolution is defined by the minimum resolvable distance between two point-scatterers. The axial resolution of an imaging system can be improved by increasing the bandwidth of the excitation waveform. To improve the lateral resolution, the aperture size of the ultrasound probe or the excitation frequency should be increased. Tissue harmonic imaging however can improve both the lateral and axial resolution of an image without changing the excitation frequency or bandwidth. A harmonic image is formed by exploiting the second harmonic generated in tissue through nonlinear propagation, which effectively has twice the center frequency and the bandwidth of the excitation waveform [1]. Another advantage of harmonic imaging is the reduced near-field artifacts, since harmonics are generated in tissue through nonlinear propagation.

Tissue harmonic imaging improves the spatial resolution by utilizing only the second harmonic; however it is possible to take advantage of higher-order harmonics and further increase the image quality. A new ultrasound imaging technique called "superharmonic imaging" was proposed in the last decade by Bouakaz *et al.* [2]. The superharmonic image is formed by combining the third, fourth, and fifth harmonic components of the received signal. These higher-order harmonic components are also produced due to the nonlinear propagation of ultrasound waves through biological tissue at high acoustic pressures [3] or due to nonlinear scattering from ultrasound contrast agents [4], [5]. It has been presented by *in vitro* and *in vivo* measurements that superharmonic imaging of biological tissue is feasible and improves the image quality [6], [7]. Bouakaz *et al.* demonstrated that contrast-enhanced superharmonic imaging increases both the contrast-to-tissue ratio and image resolution [8].

The main disadvantage of the superharmonic imaging is the requirement for a transducer with a large bandwidth and sensitivity to accommodate fundamental to fifth order harmonics of the nonlinear received signal. An interleaved phased array transducer having a $-6$ dB fractional bandwidth of $144\%$ was developed specifically for superharmonic imaging with improved transmission efficiency and higher reception sensitivity [9]. Matte *et al.* showed that the topology and frequency range of these interleaved transducers can be optimized for superharmonic imaging [10]. Use of dual frequency transducers is another option for superharmonic imaging, where Guiroy *et al.* developed a transducer for imaging of high-order nonlinear harmonics generated by microbubbles [11]. The capacitive micromachined ultrasound transducers (CMUTs) can easily achieve $>120\%$ fractional bandwidths, but usually have poor performance in terms of the output distortion and power [12]–[15]. However, recent developments in CMUT research showed that it is possible to fabricate very wideband transducers with small harmonic distortions on transmit and high pressure levels [16]–[18], making CMUTs suitable for superharmonic imaging.

Sevan Harput, James McLaughlan, David M. J. Cowell and Steven Freear are with the Ultrasound Group, School of Electronic and Electrical Engineering, University of Leeds, Leeds, LS2 9JT, UK. (E-mail: s.harput@leeds.ac.uk, s.freear@leeds.ac.uk)

Besides improving axial and lateral resolutions compared to fundamental B-mode imaging and tissue harmonic imaging, superharmonic imaging suffers from reduced signal-to-noise ratio (SNR) due to the low energy content of the higher-order nonlinear harmonic components [19], [20]. To improve the SNR and penetration depth, chirp coded excitation techniques have been used for tissue harmonic imaging instead of conventional pulsed excitation [21]–[23]. Chirp excitation has already been employed for superharmonic imaging by [24]–[26]; however their results showed that linear frequency modulated (LFM) signals underperformed due to the high sidelobe levels caused by the spectral overlap between the harmonic components.

In superharmonic imaging, the $n$-th order harmonic is located at $n$ times the center frequency of the excitation signal at $nf_0$ with a $-20$ dB bandwidth of $nB$, according to the second order distortion model [20], [27]. There will be a spectral overlap between the fourth and fifth harmonic components for any waveform that does not satisfy the following; $5f_0-4f_0 \geq (5B+4B)/2$. Therefore, signals with a fractional bandwidth narrower than $B/f_0 = 22\%$ can be filtered by using a bandpass filter as the spectral boundaries of harmonic components do not overlap. However, using excitation signals with narrow bandwidths will result in poor axial resolution. Increasing the bandwidth will cause overlapping between the harmonic components of the received signal, where the higher-order harmonics cannot be separated with conventional filtering techniques such as a bandpass filter. In the case of spectrally overlapping harmonics, signal decoding using a matched filter typically produces high range sidelobe levels, which result in image artifacts and reduce the image quality.

Various excitation schemes and imaging techniques were developed for tissue harmonic imaging to extract the harmonic component and improve the image quality such as pulse inversion, third harmonic transmit phasing, and intermodulation of ultrasound waves [28]–[32]. A dual-pulse frequency compound method was proposed to improve the image quality by improving the harmonic extraction specifically for superharmonic imaging [33], [34]. Although multi-pulse excitation methods improve the image quality, there are two main drawbacks; reduction of the system frame-rate by a factor of two, and the fact that the complete cancellation of odd-harmonic components under tissue motion cannot be achieved [21], [35]. A single-pulse compound method was recently developed by Danilouchkine *et al.* by employing two Gaussian windowed 3-cycle sine bursts with $\sim 25\%$ fractional bandwidths to avoid the spectral overlap between higher-order harmonics [36]. This method achieved a resolution comparable to the dual-pulse method by using an interleaved transducer developed by [9]. Although the maximum excitation bandwidth was limited due to spectral overlap, they had successfully performed *in vivo* superharmonic imaging of heart.

In this study, wideband linear frequency modulated chirp excitation was chosen to achieve high spatial resolution. To suppress the range sidelobes produced by spectral overlap between harmonics, a filtering technique based on the Fan Chirp transform (FChT) was applied. The FChT was employed to improve the extraction process of harmonic components overlapping both in time and frequency domains. This method was specifically designed for filtering linear frequency modulated chirps and it is not applicable to conventional pulsed excitation [37].

## II. The Fan Chirp Transform (FChT)

The Fan Chirp transform was recently introduced into chirp analysis by Képesi and Weruaga [38], [39]. It has been employed in speech analysis [38], music representation [40], signal parameter estimation [41], and time-frequency representation of the chirps [39]. However, the use of FChT has not been reported for ultrasound applications.

The name of the FChT comes from its unique *fan-shaped* transformation kernel, where the significance for this shape can be explained by comparing with other transformations. Fig. 1 represents the simplified behaviors of the Fourier transform, the fractional Fourier transform (FrFT), and the FChT on the time-frequency plane. Fig. 1(A) shows the time domain view of a chirp signal. The Fourier analysis corresponds to the sight of an observer standing orthogonal to the frequency axis at the infinite as illustrated in Fig. 1(B). In Fourier domain the time information carried by the signal is unclear. An observer standing with an angle $\phi$ to the time-frequency plane at the infinite, can see the signal's FrFT domain projection as shown in Fig. 1(C). For this case, it is possible to utilize both time and frequency information carried by the signal and the observer can achieve the best possible resolution for a linear frequency modulated chirp represented with an angle of $\phi$ on the time-frequency plane.

In order to realize the FChT, the observer must stand *inside* the time-frequency plane as represented in Fig. 1(D), where the resulting projection gives rise to the FChT spectrum. The observer can achieve the finest representation for linear frequency modulated chirps located with a fan geometry on the time-frequency plane, *i. e.* harmonically related chirps [39].

Rather than rotating the time-frequency plane as the FrFT, the FChT reshapes the time-frequency plane by twisting it into a fan geometry. Therefore, the FChT can compress a linear chirp with all of its harmonic content. This property of the FChT makes it an indispensable tool for characterization of harmonically related chirplets. Although the FrFT have been successfully used for filtering and pulse compression of LFM chirps [42]–[44], the FChT is more suitable for superharmonic imaging with chirps.

### A. The Fan Chirp Transformation Kernel

The representation of a linear frequency modulated real signal can be given as

$$s(t) = A(t) \cdot \cos(2\pi\theta(t)), \quad -\frac{T}{2} \leq t \leq \frac{T}{2} \tag{1}$$

with a phase

$$\theta(t) = \left(f_0 + \frac{\sigma}{2}t\right) t, \tag{2}$$

where $A(t)$ is the amplitude modulation function, $f_0$ is the center frequency, $B$ is the $-20$ dB bandwidth that contains the 99% of signal's total energy, $T$ is the duration of the signal, and $\sigma = B/T$ is the chirp rate.

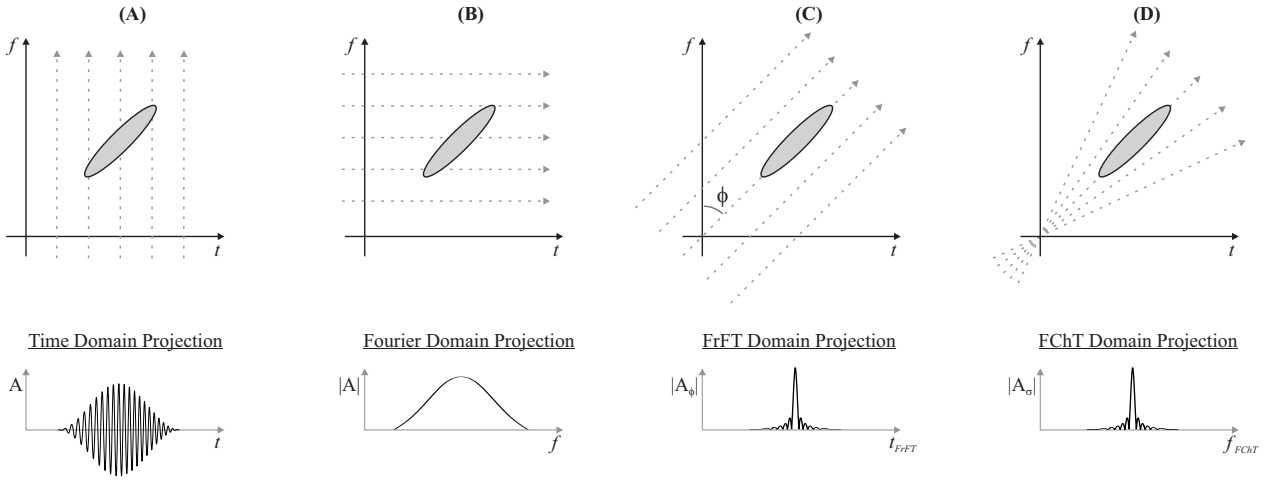


Fig. 1. (Top) Graphical explanation of (A) the Time domain, (B) the Fourier transform, (C) the Fractional Fourier transform (FrFT), (D) the Fan Chirp transform (FChT). The grey ellipse illustrates a chirp signal. The dashed arrows show the observation angle for each transformation on the time-frequency plane. (Bottom) The projection of the (A) chirp waveform in the Time domain, (B) magnitude of the signal in the Fourier domain, (C) magnitude of the signal in the FrFT domain, (D) magnitude of the signal in the FChT domain.

The Fan Chirp transform of the signal $s(t)$ can be expressed as [39]

$$S(f,\sigma) = \int_{-\infty}^{\infty} s(t)\sqrt{|\varphi'_\sigma(t)|}\, e^{-j2\pi f \varphi_\sigma(t)}\, dt, \qquad (3)$$

where $t$ is time, $f$ is frequency and $\varphi_\sigma(t)$ is the phase function or time warping function, which is controlled by the normalized chirp rate, $\sigma/f$, as

$$\varphi_\sigma(t) = \left(1 + \frac{\sigma}{2f}t\right) t. \qquad (4)$$

The $\varphi_\sigma(t)$ can be represented as the frequency normalized phase function associated with a LFM chirp with the same chirp rate as defined in Eq. (1). The $\varphi_\sigma(t)$ is equal to $\theta(t)/f$ when $f = f_0$ and the transformation kernel given in Eq. (3) matches perfectly with the signal of interest. For $f = 2f_0$, the best match for the transformation kernel will be a new chirp with twice the center frequency and chirp rate. For this case, the second harmonic component generated by the same chirp will have similar phase parameters with the FChT kernel. For any given chirp rate the FChT can achieve optimum compression including all harmonics of the chirp of interest. For $\sigma = 0$ however, the FChT kernel is the same as the Fourier transform kernel.

### *B. Filtering in the FChT Domain*

Since this study focuses on finite duration signals, for the real signal $s(t)$, centered at the origin with duration $T$, the limits of the integral in Eq. (3) reduce to $-T/2$ and $T/2$ as [41]:

$$S(f,\sigma) = \int_{-T/2}^{T/2} s(t)\sqrt{|\varphi'_\sigma(t)|}\, e^{-j2\pi f \varphi_\sigma(t)}\, dt. \qquad (5)$$

It is possible to change the limits of the integral, because the harmonics of the signal of interest are distributed on the time-frequency plane as shown in Fig. 2(top) at the same temporal location with different center frequency and bandwidths. Although computation time reduces significantly for this case, the transform needs to be calculated at different time delays.

When Eq. (5) is used for a signal longer than the duration of the excitation chirp, the process is repeated by shifting the time domain signal and computing the FChT several times to cover the whole signal length. It is similar to a running window approach, where the window length is chosen to be the duration of the excitation signal. This process is illustrated in Fig. 3(top) and the active transformation interval is highlighted between $[-T/2, T/2]$. After transforming these windowed waveforms into the FChT domain, the time delayed chirps result in frequency shifted components in the warped-frequency domain as shown in Fig. 3 middle. Therefore, the chirp signal centered at $t = 0$ will appear in the FChT domain exactly at its center frequency as shown in Fig. 3 left and right, unlike the time delayed waveforms. To differentiate between the desired waveform and time delayed waveforms a peak detection algorithm was used. The location of the spectral peak was compared with the center frequency of the chirp and delayed waveforms were discarded as given in Fig. 3(bottom).

When the FChT is computed for $\sigma/f$ according to Eq. (5), the transformation origin is located at $\langle 0, -1/(\sigma/f)\rangle$ as depicted in Fig. 2(top). For this transformation parameter, the narrowest FChT projection is achieved for all harmonics of an LFM chirp centered at $t = 0$ with a chirp rate of $\sigma$ [37]. After the transformation, the chirp and all of its harmonics appear as narrowband sinusoidal on the warped frequency domain by maintaining their center frequencies, which are shown in Fig. 2(top-middle). After achieving the optimum projection for a given chirp and its harmonics, these waveforms can be windowed in the FChT domain as represented in Fig. 2(middle).

Although, Fig. 2 and Fig. 3 explain the temporal and spectral filtering as two different methods, they were implemented together. The separation between time delayed chirps was achieved simultaneously while extracting the higher order frequency components of the same chirp signal. The higher

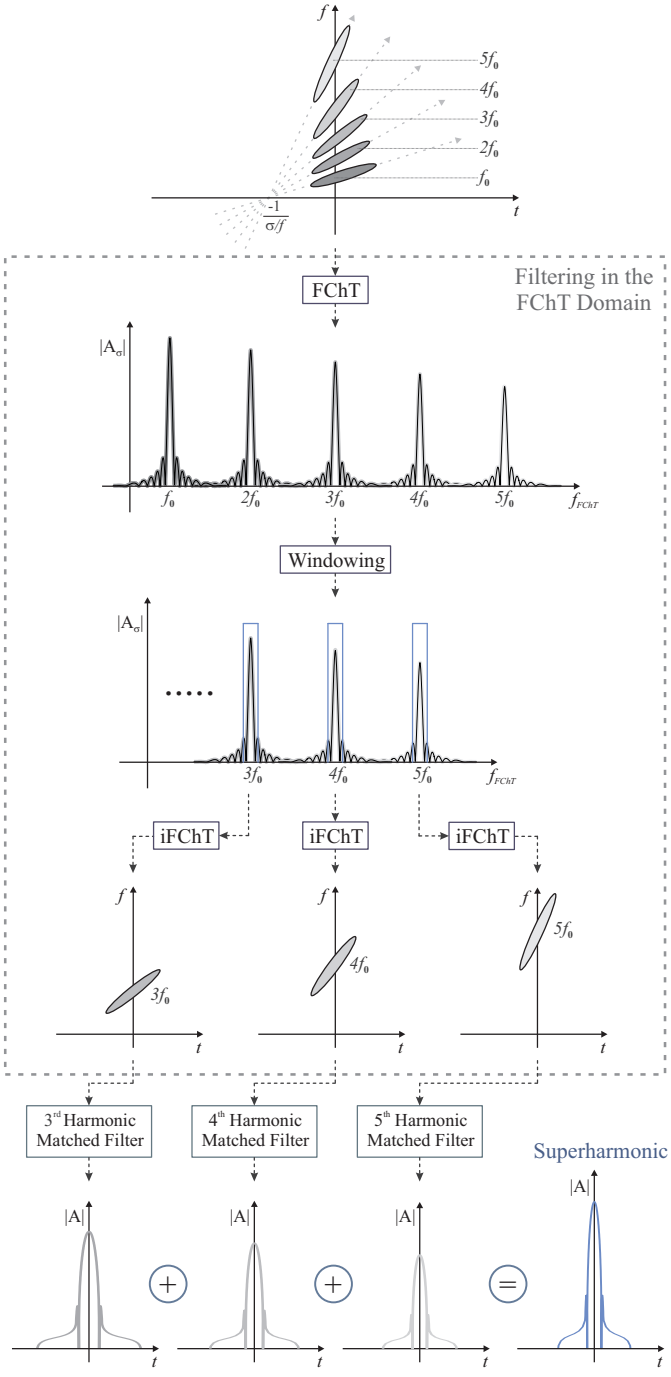


Fig. 2. Diagram illustrates the isolation of harmonically related chirps with the FChT method and formation of the superharmonic component. (Top) Time-frequency representation of harmonically related chirps. (Top-middle) Projection of these chirps in the FChT domain appears as narrowband signals at their center frequency. (Middle) Separation is achieved in the FChT domain by windowing. (Bottom-middle) Filtered chirps are shown on time-frequency plane after applying the inverse FChT. (Bottom) To calculate the superharmonic component, complex amplitudes of the third, the fourth, and the fifth harmonic components of the chirp signal are combined after pulse compression with harmonic matched filters. The absolute values are shown in this illustration for clarity.

order harmonics were not illustrated in this Fig. 3 for clarity.

After applying a window in the FChT domain, the windowed chirp and harmonics must be transformed back to the time domain by using the inverse Fan Chirp transform

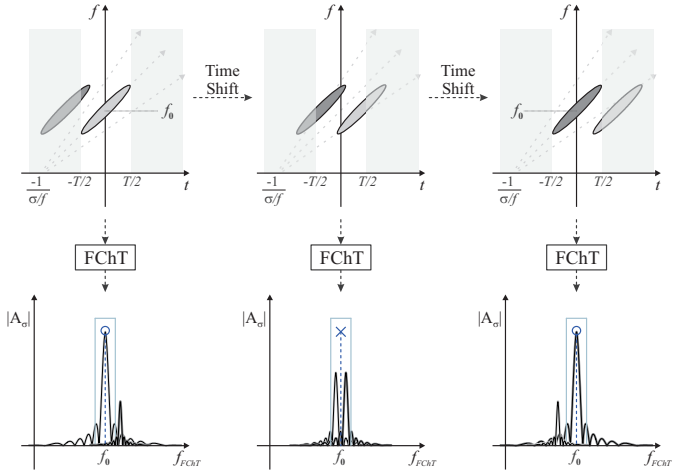


Fig. 3. Diagram illustrates the separation of time delayed waveforms using the spectral peak detection. (Top) Time-frequency representation of two chirp waveforms, where the time-frequency distribution is time shifted between the three illustrations. (Bottom) The FChT domain projection of these signals. The FChT is implemented according to Eq. (5) that only covers the time interval of $[-T/2, T/2]$. For illustrations on the left and the right, the spectral peaks are located at $f_0$, and correspond to successful transformations. The one in the middle represents a time delayed waveform that is discarded.

(iFChT), which is defined as

$$s(t) = \int_{-\infty}^{\infty} S(f,\sigma)\sqrt{|\varphi'_\sigma(t)|}\, e^{-j2\pi f \varphi_\sigma(t)}\, df. \qquad (6)$$

Separation between the spectrally overlapping harmonics can be achieved as shown in Fig. 2(bottom-middle), after applying iFChT for all individually windowed harmonics. The filtered harmonic chirps can now be compressed by a harmonic matched filter without any artifacts caused by spectral overlapping.

### C. Processing the Superharmonic Component

Individual harmonic matched filters were designed to perform pulse compression of each harmonic component. The center frequency and bandwidth of the desired harmonic matched filter were calculated by multiplying the center frequency and bandwidth of the excitation signal with that harmonic number according to the second order distortion model or square law [21], [45]. For example, the third harmonic matched filter had a center frequency of $6.75$ MHz and a $-20$ dB bandwidth of $2.7$ MHz for a chirp excitation with a center frequency of $2.25$ MHz and $40\%$ fractional bandwidth. A Hann window was applied on all harmonic matched filters as used in the excitation signal.

Extraction of the harmonic components were performed as explained in Fig. 2 with the FChT filtering and without the FChT filtering by bypassing the filtering stage. When the filtering stage is omitted, received signal in Fig. 2(top) was directly compressed with third, fourth and fifth order harmonic matched filters. The resulting complex waveforms were combined to generate the superharmonic component, where only the envelopes of the pulse compressed signals are illustrated in Fig. 2(bottom) for clarity. The superharmonic component was formed after coherent summation of pulse

compressed harmonics without normalization for both cases with or without the FChT filtering.

### D. Example

In order to show the effect of spectral overlap and the filtering capability of the FChT, a chirp waveform with harmonic content is used as an example. The harmonic components of the simulated waveform were generated to have an asymmetric wave shape and decaying harmonic power according to the wave propagation in dispersive media and weak shock theory [20]. For the sake of simplicity, it was assumed that $n^{\text{th}}$ harmonic will have $n$ times the center frequency and bandwidth (for $n = 2, 3, 4...$) and the frequency dependent attenuation was ignored. The time-frequency representation of this waveform is given in Fig. 4(top).

The fundamental component of the simulated LFM chirp has a duration of $T$, center frequency of $f_0$ and $50\%$ fractional bandwidth, which results in spectral overlap between third, fourth and fifth order harmonics, as shown in Fig. 4(top-middle).

The FrFT can achieve the narrowest projection for the fundamental or any harmonic component when the transform order is set accordingly, but not simultaneously for all harmonics. Fig. 4(bottom-middle) shows the transformation of the simulated waveform into fractional Fourier domain for the transform order that matches with the parameters of the fundamental component. The compressed fundamental component appears at $\tau_1$ and does not overlap with any of the harmonics. To extract the fundamental and harmonic components individually, the FrFT must be recalculated with a different transform order that matches with the harmonic of interest.

The FChT can achieve the narrowest projection for the fundamental and all harmonic components simultaneously. Fig. 4(bottom) shows the warped-frequency spectrum after applying the FChT, where all harmonics are clearly separated without any overlapping as observed in the Fourier and the FrFT spectra.

The importance of isolating the harmonic components for superharmonic imaging was demonstrated on the simulated waveform by comparing the range sidelobes after pulse compression. The example waveform with high harmonic content was compressed by a matched filter designed for the $n$-th harmonic component with a duration of $T$, center frequency of $n \cdot f_0$, and $50\%$ fractional bandwidth. Range sidelobes around $-30$ dB appeared on the compressed waveform for third, fourth and fifth harmonic components as shown in Fig. 5 by the light gray line. These range sidelobes caused by the spectral overlap between harmonic components are pulse compression artifacts that reduce the image quality. The dark gray line in Fig. 5 shows the final pulse compressed waveforms after separating the spectrally overlapping harmonics by filtering in the FChT domain as explained in Fig. 2. The compression artifacts and noise level were suppressed below $-80$ dB for all harmonics including the superharmonic component.

The superharmonic component has more energy and narrower $-6$ dB axial pulse width than all of the individual harmonics forming it; however the superharmonic experiences ripple artifacts due to the coherent summation of higher order harmonics as shown in Fig. 5(bottom). Ripples are caused by the spectral gap between third and fourth or fourth and fifth harmonics. When wider bandwidth ($-20$ dB FBW $\geq 100\%$) signals are used, these ripple artifacts disappear. For imaging application with a large dynamic range ($> 30$ dB), these

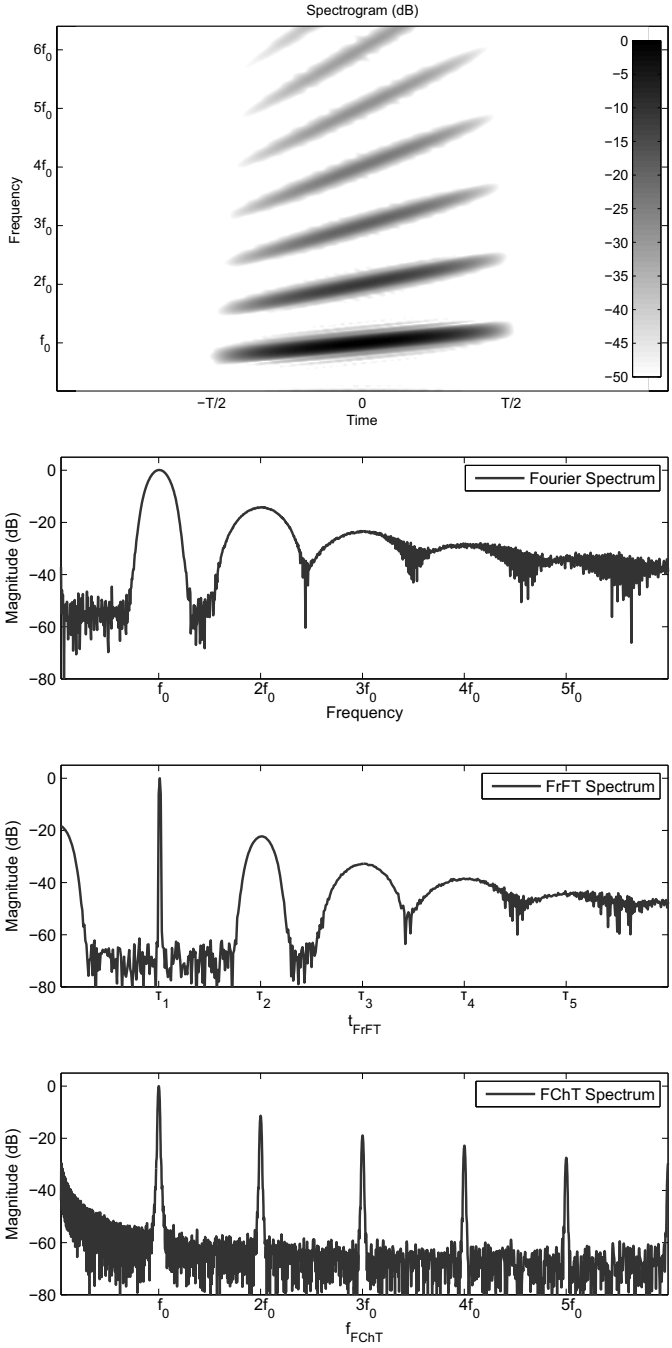


Fig. 4. Spectral plots of the simulated chirp signal with harmonic content. (Top) Spectrogram of the simulated chirp signal with harmonic content. (Top-middle) Fourier spectrum of the signal. (Bottom-middle) Fractional Fourier domain representation of the signal after applying the FrFT with a transform order that matches with the fundamental component. (Bottom) Warped-frequency domain representation of the signal after applying the FChT with a normalized chirp rate that matches with the fundamental and harmonic components.

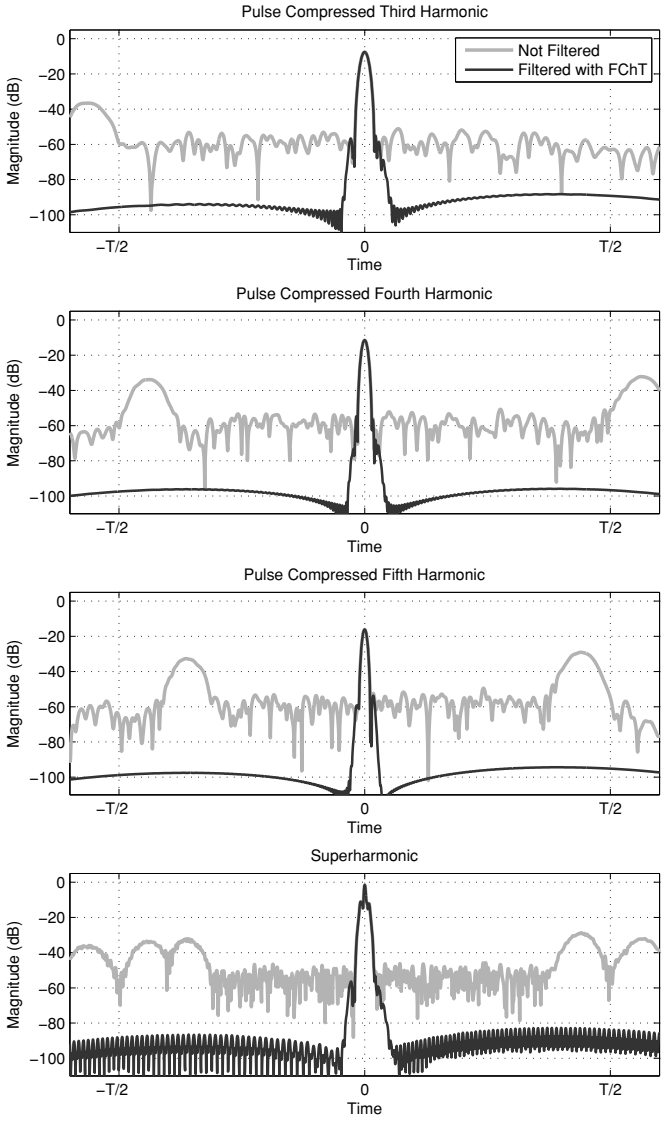


Fig. 5. Pulse compression of the simulated chirp signal with a (Top) third, (Top-middle) fourth and (Bottom-middle) fifth harmonic matched filters before and after filtering in the FChT domain. (Bottom) Superharmonic component achieved by superposition of pulse compressed third, fourth, and fifth harmonic components processed with and without the FChT filtering.

ripples will be barely visible on the gray scale image.

## III. Materials and Methods

To verify the accuracy of the proposed filtering technique, several measurements were performed by capturing the harmonics generated due to the nonlinear propagation of ultrasound waves in water. Measurements were performed for excitation waveforms with varying bandwidths to show the effect of spectral overlap. After demonstrating the filtering capability of the FChT, the superharmonic image of a wire phantom was acquired by using a focused transducer and a focused hydrophone.

### A. Harmonic Measurements

Measurements were performed in a tank containing deionized and degassed water at $19\pm1^{\circ}$C as illustrated in Fig. 6. The transducer and hydrophone were aligned coaxially in a pitch-catch configuration. An axial scan was performed for different depths using a custom built computer numerical control (CNC) system.

Five different LFM chirps were transmitted with a center frequency of 2.25 MHz, duration of 20 $\mu$s, and fractional bandwidths (FBWs) of 10, 20, 30, 40, and 50%. A Hann window was used to shape the envelope of the signal $A(t)$ to improve the sidelobe performance and reduce the spectral leakage [46]. A 33250A Arbitrary Waveform Generator (Agilent Technologies Inc., Santa Clara, CA) was set to generate excitation signals. The signals were amplified by an A150 RF Power Amplifier (Electronics & Innovation Ltd., Rochester, NY). The amplified chirp signals were transmitted by a 2.25 MHz single element V323-SM immersion transducer (Olympus-NDT Inc., Waltham, MA) with 56% fractional bandwidth. The radiating surface of transducer was a flat, which resulted in a weakly focused ultrasound beam at far-field around 15 mm.

After nonlinear propagation in water, signals were detected using a Polyvinylidene Fluoride (PVDF) differential membrane hydrophone (Precision Acoustics Ltd., Dorchester, UK). The peak positive and the peak negative pressure levels of each waveform at 2.25 MHz at the focus of the transducer were 1.125 MPa and 1 MPa, respectively. The received signals were acquired at 1 GSpS sampling rate using a Waverunner 44xi oscilloscope (LeCroy Corporation, Chestnut Ridge, NY) with 100-times averaging to improve the SNR. The captured data was processed offline in Matlab (MathWorks Inc., Natick, MA).

### B. Superharmonic Imaging Setup

A wire phantom was built to show the effectiveness of the proposed algorithm for superharmonic imaging. There is no commercial transducer available to replicate the measurements performed in the previous section in pulse-echo mode, in terms of bandwidth and sensitivity. Therefore a focused transducer and a focused hydrophone were used to imitate a B-scan. A two-dimensional scan of the wire phantom was performed with the same CNC system as illustrated in Fig. 8. This phantom consisted of seven aluminum wires with a diameter of 120 $\mu$m stretched across two parallel plates in water. The geometry of the wire phantom is shown on the right in Fig. 8.

A H-102 high-intensity focused ultrasound (HIFU) transducer (Sonic Concepts Inc., Bothell, WA) with a 20 mm central opening was used as a transmitter. Outer and inner diameters of the HIFU active element were 64 mm and 22.6 mm, respectively. The HIFU transducer had a geometric focus of 63.2 mm from the curvature of radiating surface. A Y-107 focused hydrophone (Sonic Concepts Inc., Bothell, WA) with an active diameter of 17.5 mm was fit into the central opening with a geometric focal depth of 64 mm. The hydrophone had an operating frequency range of 10 kHz-15 MHz with a sensitivity of 25.6 V/MPa at 10 MHz.

The HIFU transducer had a center frequency of 1.1 MHz and a fractional bandwidth of 63%. An A300 RF Power Amplifier (Electronics & Innovation Ltd., Rochester, NY) was used to excite the HIFU transducer by amplifying a

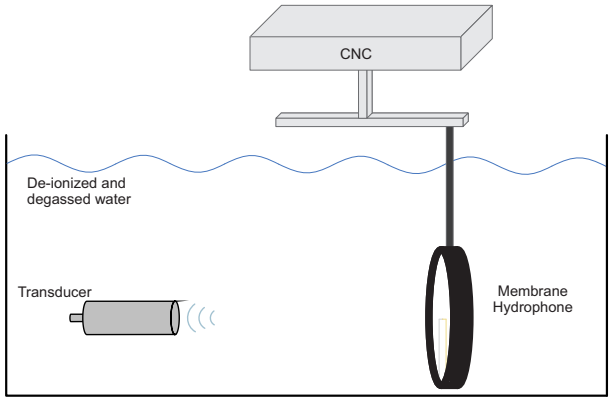


Fig. 6. Schematic diagram of the measurement setup used for capturing the harmonics generated in water. Measurements were performed in a tank filled with de-ionized and degassed water. The 2.25 MHz transducer was used to transmit different chirp waveforms, which were received by the membrane hydrophone after nonlinear propagation in water. The alignment of the transducer and the membrane hydrophone was performed by a CNC system.

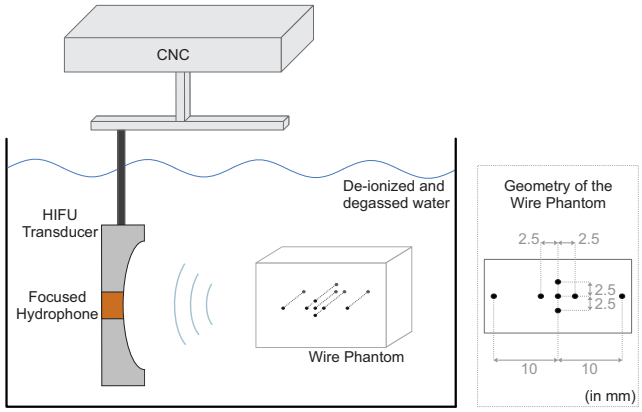


Fig. 8. Schematic diagram of the imaging setup. The wire phantom was scanned with a CNC system by using the HIFU transducer as a transmitter and the focused hydrophone as a receiver. Dimensions of the wire phantom are given in millimeters on the right.

Hann windowed chirp waveform with a center frequency of 1.1 MHz, duration of 20 $\mu$s, and fractional bandwidth of 50%. The peak negative pressure at the focus of the HIFU transducer was 1.99 MPa, which corresponds to a mechanical index (MI) of 1.9.

Reflected echoes were detected using the focused hydrophone. The received signals were acquired with a sampling frequency of 500 MHz using the LeCroy Waverunner digital oscilloscope. The captured data was processed offline in Matlab.

## IV. Experimental Results and Discussion

A set of measurements were performed to capture the harmonics generated due to the nonlinear propagation in water as shown in Fig. 6. The pressure field was measured between the depths of $20 - 100$ mm, where the maximum energy transfer to the superharmonic component was achieved at 86 mm. The received signals at this depth and their associated power spectra are shown in Fig. 7. This figure shows the shock-wave formation, distortion in signal symmetry, and the generation of higher-order harmonics due to the nonlinear propagation at high acoustic pressure. It can also be observed that increasing the bandwidth of the excitation will increase the bandwidth of the harmonics, which results in overlapping between higher-order harmonic components.

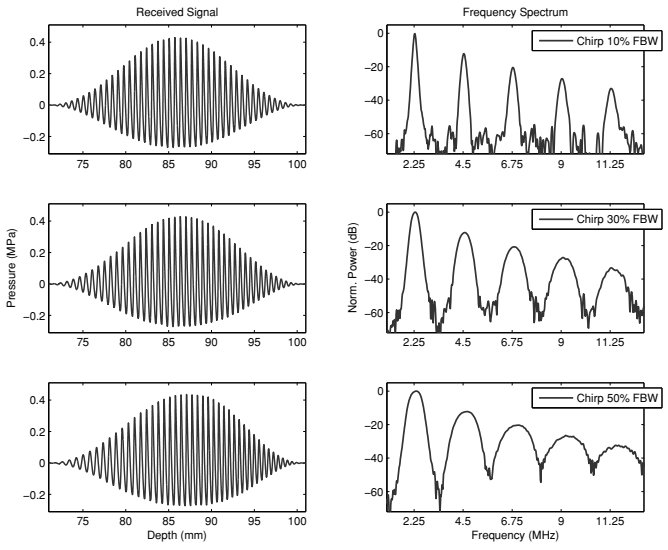


Fig. 7. (Left) Received signals at the same depth for different excitation waveforms and (Right) the associated power spectra showing the harmonic content of the received signals. (Top) Chirp excitation with 10%, (Middle) 30%, and (Bottom) 50% fractional bandwidths were given to show the increase in spectral overlapping for higher-order harmonics generated by waveforms with wider bandwidths.

### A. Without Filtering in the FChT Domain

A comparison of the processed superharmonic components showed that the excitation with greater bandwidth achieved better axial resolution, as shown in Fig. 9. The performance of the superharmonic for the chirp excitation was close to the theoretical expectations, where increasing the signal bandwidth proportionally improved the axial resolution. A detailed comparison of axial resolution measured at $-20$ dB of the mainlobe width is given in Table I for all harmonic components. Since these pulse compressed waveforms were being compared for an imaging application, $-20$ dB mainlobe width was preferred instead of full-width-at-half-maximum ($-6$ dB mainlobe width).

The superharmonic extracted from all chirp excitations provided around 30% improvement in axial resolution when compared with second harmonic components of the same bandwidth. The improvement in resolution demonstrates that chirp excitation and harmonic matched filters are good candidates for harmonic imaging. The comparison of the superharmonic components for different bandwidths are given Fig. 9. In this figure around 10 $\mu$s, range sidelobes as high as $-33$ and $-23$ dB appear for superharmonic components of chirps with 40% and 50% fractional bandwidths, respectively. There is also a pulse compression artifact expected around 11 $\mu$s for the superharmonic component of the chirp excitation with 30% FBW, which is not clearly visible in the Fig. 9 due to noise. This artifact appears around $-50$ dB level, which is

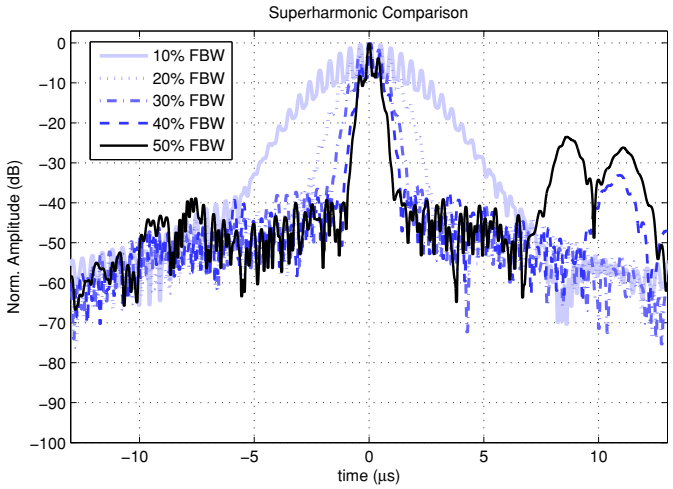


Fig. 9. Comparison of the superharmonic components obtained by chirp excitations with 10%, 20%, 30%, 40%, and 50% fractional bandwidths without filtering in the FChT domain.

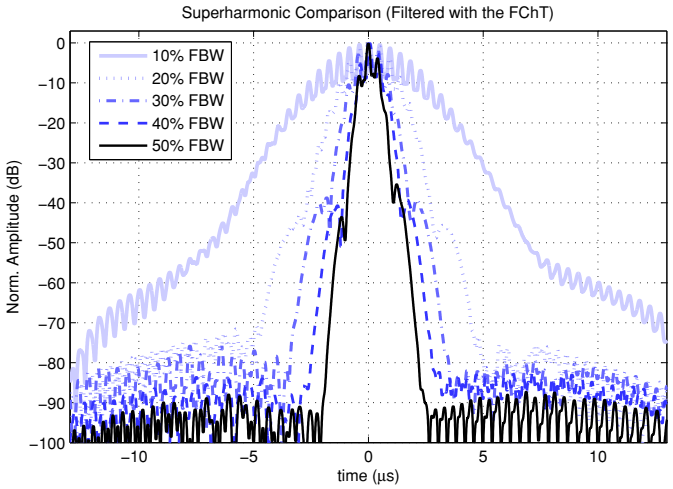


Fig. 10. Comparison of the superharmonic components obtained by chirp excitations with 10%, 20%, 30%, 40%, and 50% fractional bandwidths after filtering in the FChT domain as explained in Fig. 2.

TABLE I
−20 dB Axial Pulse Width

| | Pulse Width ($\mu$s) | | | | |
|---|---|---|---|---|---|
| | 10% | 20% | 30% | 40% | 50% |
| 2nd Harmonic | 11.31 | 5.60 | 3.68 | 2.73 | 2.16 |
| 3rd Harmonic | 8.57 | 4.23 | 2.75 | 2.05 | 1.62 |
| 4th Harmonic | 6.95 | 3.47 | 2.24 | 1.66 | 1.32 |
| 5th Harmonic | 6.16 | 3.23 | 1.98 | 1.43 | 1.16 |
| Superharmonic | 7.87 | 3.98 | 2.55 | 1.89 | 1.50 |

TABLE II
−20 dB Axial Pulse Width after filtering with the FChT

| | Pulse Width ($\mu$s) | | | | |
|---|---|---|---|---|---|
| | 10% | 20% | 30% | 40% | 50% |
| 2nd Harmonic | 11.30 | 5.60 | 3.68 | 2.73 | 2.16 |
| 3rd Harmonic | 8.57 | 4.23 | 2.75 | 2.05 | 1.63 |
| 4th Harmonic | 6.94 | 3.46 | 2.24 | 1.66 | 1.32 |
| 5th Harmonic | 6.13 | 3.19 | 1.98 | 1.43 | 1.16 |
| Superharmonic | 7.84 | 3.96 | 2.54 | 1.88 | 1.50 |

acceptably low for imaging applications.

Improvements achieved by superharmonic component are shadowed by the ripple artifacts for narrowband excitation, which can be observed in Fig. 9 for chirps with 10% and 20% fractional bandwidths. Therefore, the wideband excitation, which is the chirp with 50% fractional bandwidth for this study, is the best candidate for superharmonic imaging.

Despite improving the axial resolution, the superharmonic component will always suffer from high range sidelobe levels due to spectral overlap between the higher-order harmonics for wideband excitation above the theoretical limit of 22% FBW. Several recent studies have used chirps for superharmonic imaging and achieved results similar to those presented in this section [24]–[26].

### B. After Filtering in the FChT Domain

In order to improve the previous results and reduce the range sidelobe levels, the FChT was employed to filter the spectrally overlapped chirps. Received signals were transformed to the FChT domain and all harmonics were individually filtered. The bandwidth of the filtering window was selected according to the SNR of the experimental measurements, which was $-70$ dB width of the autocorrelation function of the excitation waveform [37]. The extracted harmonics were transformed back to the time domain by using the iFChT and compressed by a harmonic matched filter as explained in Fig. 2.

Although peak sidelobe levels stayed the same, the range sidelobes after pulse compression were improved for all excitation waveforms, which can be observed in Fig. 10. The improvement achieved by using the FChT is $> 50$ dB for range sidelobes of chirp excitation with 40% and 50% FBWs.

No degradation was observed on the axial resolution, since the signal bandwidth was not changed. Results for signals processed with and without the FChT filtering are $\pm 0.04$ $\mu$s in agreement with each other as given in Table I and Table II. Comparing Fig. 9 and Fig. 10 shows improvement of the range sidelobe levels after using the FChT for filtering the spectrally overlapped harmonic chirps without reducing the axial resolution.

### C. Superharmonic Imaging of the Wire Phantom

Fundamental, second harmonic and superharmonic images of the wire phantom are shown in Fig. 11 and Fig. 12. Both fundamental images with or without filtering in the FChT domain suffered from poor resolution and lateral artifacts. These artifacts appear as white shadows around wires in lateral direction due to the shape of the ultrasound beam generated by the HIFU transducer. For example, in Fig. 11(top) for the first wire located at $(20, 0)$ there are two lateral artifacts appearing at $(20, -2)$ and $(20, 2)$. The spatial sidelobes of the HIFU beam match with the calibration data supplied by the manufacturer. Dark stripes between these artifacts and main scatterers are due to the zero nodes between the main lobe and the lateral sidelobes in the radiation pattern of HIFU transducer. These artifacts can be avoided by using an

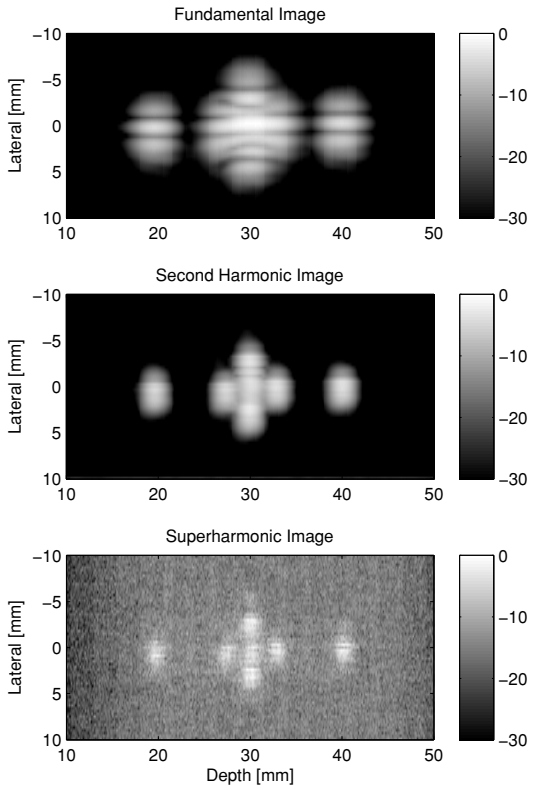


Fig. 11. (Top) Fundamental, (Middle) second harmonic and (Bottom) superharmonic images of the wire phantom. The fundamental and second harmonic images were formed after pulse compression with a matched filter and second harmonic matched filter, respectively. The superharmonic image was formed by processing the received signal without the FChT filtering as explained in Fig. 2 by bypassing the filtering stage.

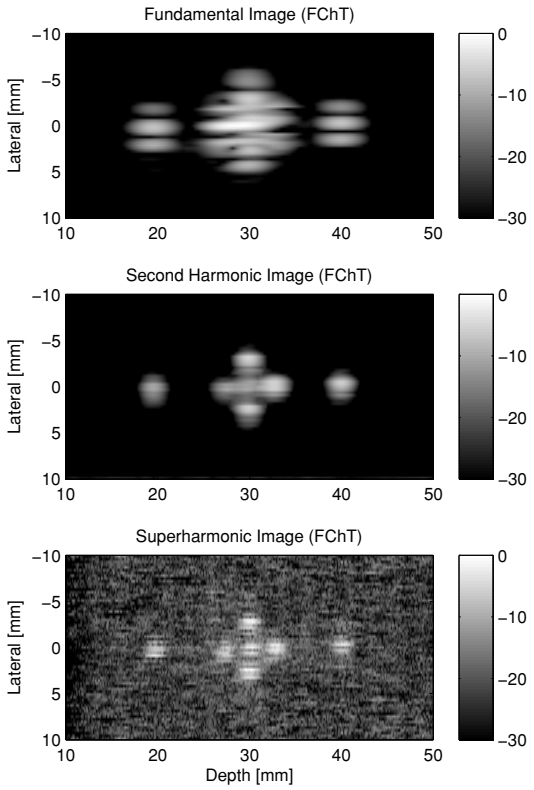


Fig. 12. (Top) Fundamental, (Middle) second harmonic and (Bottom) superharmonic images of the wire phantom filtered with the FChT technique before pulse compression. The fundamental and second harmonic images were formed after filtering with the FChT and then compressing with a matched filter and second harmonic matched filter, respectively. The superharmonic image was formed by processing the received signal as explained in Fig. 2.

array transducer with an array apodization, instead of using a single element HIFU transducer that mechanically scans the imaging field. For the second harmonic, the beam shape at the focal region gets smaller and sidelobes disappear. Therefore, second harmonic images have nearly two times higher spatial resolution compared to the fundamental images.

When the fundamental and second harmonic images processed without the FChT in Fig. 11(top) and (middle) were compared to images filtered with the FChT in Fig. 12(top) and (middle), an improvement in lateral resolution is also observed. The reason for this improvement is due to the existence of a time delay between the direct reflections and scattered or diffracted waves from a point reflector arriving with an angle. The FChT algorithm is capable of removing these indirect reflections, since time delays introduce a frequency shift in the FChT domain and therefore filtered out after windowing. By filtering with the FChT technique, an average improvement of 30% and 40% in lateral resolution was observed for the fundamental and second harmonic images, respectively.

For superharmonic imaging, noise and artifact levels were reduced from $-14$ dB in Fig. 11(bottom) to $-21$ dB in Fig. 12(bottom) after filtering with the FChT. This improvement effectively increases the image dynamic range, however here both images were plotted with a 30 dB dynamic range for a fair comparison. After the improvement achieved by the FChT filtering method, the central wire located at $(30, 0)$ can be resolved from the superharmonic image given in Fig. 12(bottom).

The improvement achieved by filtering with the FChT was only 7 dB for this imaging setup because of two reasons. First, used equipment were limited with $14 \pm 6$ dB SNR at the superharmonic frequency range for the given excitation parameters. Therefore, the range sidelobe suppression could not be demonstrated on a wire phantom, where the average noise level was around $-14$ dB in Fig. 11(bottom). The range sidelobe levels of the superharmonic component for $50\%$ FBW chirp excitation were expected to be around $-23$ dB as presented in Fig. 9, which is well below the noise floor and thus not visible in the superharmonic image. Second, the generation of higher-order harmonics were limited due to the low center frequency of the HIFU transducer and MI limitation of 1.9 for medical ultrasound imaging [47].

By using a similar transducer and receiver pair working at a higher frequency range, such as the transducer designed by Guiroy *et al.* [11], the benefits of the FChT filtering technique become increasingly significant. When the excitation frequency is increased, more harmonics will be generated due to nonlinear propagation at the same acoustic pressure level and depth. Also the excitation pressure can be increased, since MI is inversely proportional with the square root of the excitation frequency [48].

The separation methodology of chirps with time-frequency

overlaps as explained in Fig. 2 and Fig. 3 was presented on a wire phantom; however tissue will create a more complicated problem. In tissue, scatterers are distributed at all depths without a clear time separation. Although, separation of temporally overlapping chirps is possible [42], the main issue will be filtering the spectral overlap between different order of harmonics of closely spaced scatterers. For example, when the third harmonic of a scatterer located at $t = t_1$ and the fourth harmonic of a scatterer located at $t = t_2$ intersect in time-frequency plane, where $t_2 - t_1 << T$, the FChT is not able to recover this signal accurately. However, filtering these overlaps is also a big signal processing challenge for time and frequency filtering based on convolution and recursion.

## V. Conclusions

The main advantage of the superharmonic imaging over second harmonic imaging is the enhanced spatial resolution. This improvement on lateral and axial resolution was confirmed in biological tissues with simulations and experiments by Ma *et al.* [7]. Experimental measurements performed in this work verify these previous results. When the superharmonic components were compared with the second harmonic components, an average of 30% improvement was observed for all chirp excitations as given in Table I and Table II.

Another less pronounced advantage of the superharmonic imaging is the compounding effect. Combining different harmonic components gives benefits similar to those of frequency compounding [49]. Therefore, significant reduction in speckle size can be achieved by superharmonic imaging and more details can be visualized. For this reason, superharmonic imaging is a good candidate for all types of medical imaging applications where high image resolution is necessary such as detection of small lesions, ophthalmic ultrasound, and small animal imaging [50], [51].

Contrast-enhanced ultrasound imaging is another modality that can benefit from the use of higher-order harmonics. Bouakaz *et al.* demonstrated that the contrast-to-tissue ratio (CTR) increases as a function of harmonic order even at low MI ($< 0.4$) [2]. For super harmonic imaging with chirps, long duration chirp excitation amplifies the microbubble response and offers an improved CTR, but the resonance behavior of microbubbles introduce new complications for imaging applications. Nevertheless, the FChT can still be used for filtering and separating harmonically related chirps. From a signal processing aspect, microbubbles alter the phase, the envelope shape, and the frequency content of the scattered echoes that make filtering even more challenging for contrast-enhanced ultrasound imaging with chirps. Also the phase coherence between different orders of harmonics is not necessarily preserved for harmonics generated by microbubbles [52], where pulse inversion and pulse sequences will not achieve the optimum performance. However, the scattered response from the microbubble population still have the same chirp rate as the excitation signal and the chirp rate of the harmonics generated by the microbubbles are scaled by a ratio of $n$ for the $n$-th harmonic [37]. Frequency dependent attenuation, which is common in every type of ultrasound imaging application, causes a down-shift in the frequency response but does not alter the chirp rate. Therefore, it is possible to use the FChT as a filtering tool for superharmonic imaging even with ultrasound contrast agents, since the transformation is sensitive to signal's chirp rate.

Although superharmonic imaging improves the image quality, the spectral overlap between the higher-order harmonics introduces image artifacts and reduces the dynamic range. Pulse inversion cannot be used to separate the overlapping harmonics, since it will cancel out all the odd harmonics. New multiple excitation methods were proposed specifically for superharmonic imaging such as the dual-pulse method offered by van Neer *et al.* [34]. This approach can generate higher-quality harmonic images at the cost of a reduced frame rate, but it cannot be applied to coded excitation. Conventional bandpass filtering can separate the harmonic components at the expense of reduced bandwidth. To overcome these limitations, a new filtering method based on the FChT was designed in order to separate the spectrally overlapped harmonic components without sacrificing the signal bandwidth and frame rate. When the direct form FChT is compared with a filtering method based on fast Fourier transform (FFT) in terms of speed, the FChT performs three orders of magnitude slower. However, the fast FChT can be implemented as the Fourier transform of a time warped signal, which makes the speed dependent to the applied interpolation algorithm for time warping. Weruaga and Képesi performed an analysis on computing requirements for the fast FChT and approximated the computational complexity as $N(7+\log(N))$ [39]. Dunn *et al.* demonstrated that the choice of interpolation method gives a trade-off between the computational speed and the accuracy of the transformation [41]. When the fast FChT is applied with the *pchip* interpolation method in Matlab, it is only an order of magnitude slower than the FFT and can be used for real-time imaging.

The main limitations of the superharmonic imaging are the transducer sensitivity, low SNR, and reduced penetration depth. The higher-order harmonics are usually located at a frequency band where the transducer does not work efficiently, therefore causing a reduction in the SNR and sensitivity. The penetration depth is reduced because of frequency-dependent attenuation in tissue. In this study, the SNR and penetration were improved by using coded excitation and increasing the total transmitted energy, but the available transducer bandwidth is still the biggest limitation for the superharmonic imaging. The commercial ultrasound probes do not have sufficient bandwidth; however the research on transducer and CMUT technology is focusing on increasing the transducer bandwidth and reception sensitivity [9]–[11], [15], [17], [18], [53], [54]. With the availability of very broad bandwidth (>150%) and dual frequency transducers, the superharmonic imaging can become a standard modality for high resolution imaging in the future.

## Acknowledgment

This work was supported by EPSRC grant EP/K029835/1.

## REFERENCES


[1] F. Tranquart, N. Grenier, V. Eder, and L. Pourcelot, "Clinical use of ultrasound tissue harmonic imaging," *Ultrasound in Medicine & Biology*, vol. 25, no. 6, pp. 889–894, 1999.

[2] A. Bouakaz, S. Frigstad, F. J. T. Cate, and N. de Jong, "Super harmonic imaging: a new imaging technique for improved contrast detection," *Ultrasound in Medicine & Biology*, vol. 28, no. 1, pp. 59–68, 2002.

[3] F. A. Duck, "Nonlinear acoustics in diagnostic ultrasound," *Ultrasound in Medicine & Biology*, vol. 28, no. 1, pp. 1–18, 2002.

[4] K. E. Morgan, P. A. Dayton, D. E. Kruse, A. L. Klibanov, G. H. Brandenburger, and K. W. Ferrara, "Changes in the echoes from ultrasonic contrast agents with imaging parameters," *Ultrasonics, Ferroelectrics and Frequency Control, IEEE Transactions on*, vol. 45, no. 6, pp. 1537–1548, 1998.

[5] N. de Jong, A. Bouakaz, and P. Frinking, "Basic acoustic properties of microbubbles," *Echocardiography*, vol. 19, no. 3, pp. 229–240, 2002.

[6] A. Bouakaz and N. de Jong, "Native tissue imaging at superharmonic frequencies," *Ultrasonics, Ferroelectrics and Frequency Control, IEEE Transactions on*, vol. 50, no. 5, pp. 496–506, 2003.

[7] Q. Ma, D. Zhang, X. Gong, and Y. Ma, "Investigation of superharmonic sound propagation and imaging in biological tissues in vitro," *The Journal of the Acoustical Society of America*, vol. 119, no. 4, pp. 2518–2523, 2006.

[8] A. Bouakaz, B. J. Krenning, W. B. Vletter, F. J. ten Cate, and N. de Jong, "Contrast superharmonic imaging: A feasibility study," *Ultrasound in Medicine & Biology*, vol. 29, no. 4, pp. 547–553, 2003.

[9] P. L. M. J. van Neer, G. Matte, M. G. Danilouchkine, C. Prins, F. Van Den Adel, and N. de Jong, "Super-harmonic imaging: development of an interleaved phased-array transducer," *Ultrasonics, Ferroelectrics and Frequency Control, IEEE Transactions on*, vol. 57, no. 2, pp. 455–468, 2010.

[10] G. Matte, P. L. M. J. van Neer, M. Danilouchkine, J. Huijssen, M. Verweij, and N. de Jong, "Optimization of a phased-array transducer for multiple harmonic imaging in medical applications: frequency and topology," *Ultrasonics, Ferroelectrics and Frequency Control, IEEE Transactions on*, vol. 58, no. 3, pp. 533–546, 2011.

[11] A. Guiroy, A. Novell, E. Ringgaard, R. Lou-Moeller, J.-M. Gregoire, A.-P. Abellard, T. Zawada, A. Bouakaz, and F. Levassort, "Dual-frequency transducer for nonlinear contrast agent imaging," *Ultrasonics, Ferroelectrics and Frequency Control, IEEE Transactions on*, vol. 60, no. 12, pp. 2634–2644, 2013.

[12] D. Mills, "Medical imaging with capacitive micromachined ultrasound transducer (cmut) arrays," in *IEEE Ultrasonics Symposium*, vol. 1, 2004, pp. 384–390.

[13] S. Olcum, M. Senlik, and A. Atalar, "Optimization of the gain-bandwidth product of capacitive micromachined ultrasonic transducers," *Ultrasonics, Ferroelectrics and Frequency Control, IEEE Transactions on*, vol. 52, no. 12, pp. 2211–2219, 2005.

[14] A. Logan and J. T. W. Yeow, "Fabricating capacitive micromachined ultrasonic transducers with a novel silicon-nitride-based wafer bonding process," *Ultrasonics, Ferroelectrics and Frequency Control, IEEE Transactions on*, vol. 56, no. 5, pp. 1074–1084, 2009.

[15] J. Park, X. Li, Q. Zhou, and K. K. Shung, "Combined chirp coded tissue harmonic and fundamental ultrasound imaging for intravascular ultrasound: 2060 mhz phantom and ex vivo results," *Ultrasonics*, vol. 53, no. 2, pp. 369–376, 2013.

[16] A. Novell, S. Der Meer, M. Versluis, N. Jong, and A. Bouakaz, "Contrast agent response to chirp reversal: simulations, optical observations, and acoustical verification," *Ultrasonics, Ferroelectrics and Frequency Control, IEEE Transactions on*, vol. 56, no. 6, pp. 1199–1206, 2009.

[17] S. Satir and F. L. Degertekin, "Harmonic reduction in capacitive micromachined ultrasonic transducers by gap feedback linearization," *Ultrasonics, Ferroelectrics and Frequency Control, IEEE Transactions on*, vol. 59, no. 1, pp. 50–59, 2012.

[18] F. Y. Yamaner, S. Olcum, H. K. Oguz, A. Bozkurt, H. Koymen, and A. Atalar, "High-power cmuts: Design and experimental verification," *Ultrasonics, Ferroelectrics and Frequency Control, IEEE Transactions on*, vol. 59, no. 6, pp. 1276–1284, 2012.

[19] P. L. M. J. van Neer, M. G. Danilouchkine, M. D. Verweij, L. Demi, M. M. Voormolen, A. F. W. van der Steen, and N. de Jong, "Comparison of fundamental, second harmonic, and superharmonic imaging: A simulation study," *The Journal of the Acoustical Society of America*, vol. 130, no. 5, pp. 3148–3157, 2011.

[20] M. F. Hamilton and D. T. Blackstock, *Nonlinear Acoustics*. Acoustical Society of America, 2008.

[21] R. Arshadi, A. C. H. Yu, and R. S. C. Cobbold, "Coded excitation methods for ultrasound harmonic imaging," *Canadian Acoustics*, vol. 35, no. 2, pp. 35–46, 2007.

[22] J. Song, S. Kim, H.-Y. Sohn, T.-K. Song, and Y. M. Yoo, "Coded excitation for ultrasound tissue harmonic imaging," *Ultrasonics*, vol. 50, no. 6, pp. 613–619, 2010.

[23] C.-C. Shen and C.-H. Lin, "Chirp-encoded excitation for dual-frequency ultrasound tissue harmonic imaging," *Ultrasonics, Ferroelectrics and Frequency Control, IEEE Transactions on*, vol. 59, no. 11, pp. 2420–2430, 2012.

[24] M. Arif, S. Harput, and S. Freear, "Experimental investigation of chirp coded excitation in ultrasound superharmonic imaging," in *IEEE Ultrasonics Symposium*, 2010, pp. 2187–2190.

[25] M. G. Danilouchkine, P. L. M. J. van Neer, G. M. Matte, M. M. Voormolen, M. D. Verweij, and N. de Jong, "Superharmonic imaging based on chirps," in *IEEE Ultrasonics Symposium*, 2010, pp. 2195–2198.

[26] P. van Neer, M. G. Danilouchkine, G. Matte, M. M. Voormolen, M. D. Verweij, , and N. de Jong, "Feasibility study of superharmonic imaging using chirps," in *Proceedings of Meetings on Acoustics*, vol. 9, no. 020001, 2010.

[27] R. S. C. Cobbold, *Foundations of Biomedical Ultrasound*. Oxford University Press, 2007.

[28] P. N. Burns, S. R. Wilson, and D. H. Simpson, "Pulse inversion imaging of liver blood flow: Improved method for characterizing focal masses with microbubble contrast," *Investigative Radiology*, vol. 35, no. 1, pp. 58–71, 2000.

[29] Q. Ma, Y. Ma, X. Gong, and D. Zhang, "Improvement of tissue harmonic imaging using the pulse-inversion technique," *Ultrasound in Medicine & Biology*, vol. 31, no. 7, pp. 889–894, 2005.

[30] C.-C. Shen, Y.-C. Wang, and Y.-C. Hsieh, "Third harmonic transmit phasing for tissue harmonic generation," *Ultrasonics, Ferroelectrics and Frequency Control, IEEE Transactions on*, vol. 54, no. 7, pp. 1370–1381, 2007.

[31] E. Biagi, L. Breschi, E. Vannacci, and L. Masotti, "Multipulse technique exploiting the intermodulation of ultrasound waves in a nonlinear medium," *Ultrasonics, Ferroelectrics and Frequency Control, IEEE Transactions on*, vol. 56, no. 3, pp. 520–535, 2009.

[32] D. M. J. Cowell, P. R. Smith, and S. Freear, "Phase-inversion-based selective harmonic elimination (PI-SHE) in multi-level switched-mode tone- and frequency- modulated excitation," *Ultrasonics, Ferroelectrics and Frequency Control, IEEE Transactions on*, vol. 60, no. 6, pp. 1084–1097, 2013.

[33] G. M. Matte, P. L. M. J. van Neer, J. M. G. Borsboom, M. D. Verweij, and N. de Jong, "A new frequency compounding technique for super harmonic imaging," in *IEEE Ultrasonics Symposium*, 2008, pp. 357–360.

[34] P. L. M. J. van Neer, M. G. Danilouchkine, G. M. Matte, A. F. W. van der Steen, and N. de Jong, "Dual-pulse frequency compounded superharmonic imaging," *Ultrasonics, Ferroelectrics and Frequency Control, IEEE Transactions on*, vol. 58, no. 11, pp. 2316–2324, 2011.

[35] C.-C. Shen and P.-C. Li, "Motion artifacts of pulse inversion-based tissue harmonic imaging," *Ultrasonics, Ferroelectrics and Frequency Control, IEEE Transactions on*, vol. 49, no. 9, pp. 1203–1211, 2002.

[36] M. G. Danilouchkine, P. L. M. J. van Neer, M. D. Verweij, G. M. Matte, W. B. Vletter, A. F. W. van der Steen, and N. de Jong, "Single pulse frequency compounding protocol for superharmonic imaging," *Physics in Medicine and Biology*, vol. 58, no. 14, pp. 4791–4805, 2013.

[37] S. Harput, "Use of chirps in medical ultrasound imaging," Ph.D. Thesis, School of Electronic and Electrical Engineering, University of Leeds, UK, 2012.

[38] M. Képesi and L. Weruaga, "Adaptive chirp-based timefrequency analysis of speech signals," *Speech Communication*, vol. 48, no. 5, pp. 474–492, 2006.

[39] L. Weruaga and M. Képesi, "The fan-chirp transform for non-stationary harmonic signals," *Signal Processing*, vol. 87, no. 6, pp. 1504–1522, 2007.

[40] P. Cancela, E. López, and M. Rocamora, "Fan chirp transform for music representation," in *Proc of the 13th Int Conference on Digital Audio Effects*, 2010, pp. 1–8.

[41] R. B. Dunn, T. F. Quatieri, and N. Malyska, "Sinewave parameter estimation using the fast fan-chirp transform," in *IEEE Workshop on Applications of Signal Processing to Audio and Acoustics*, 2009, pp. 349–352.

[42] S. Harput, T. Evans, N. Bubb, and S. Freear, "Diagnostic ultrasound tooth imaging using fractional Fourier transform," *Ultrasonics, Ferroelectrics and Frequency Control, IEEE Transactions on*, vol. 58, no. 10, pp. 2096–2106, 2011.

[43] M. Arif, D. M. J. Cowell, and S. Freear, "Pulse compression of harmonic chirp signals using the fractional Fourier transform," *Ultrasound in Medicine & Biology*, vol. 36, no. 6, pp. 949–956, 2010.

[44] D. M. J. Cowell and S. Freear, "Separation of overlapping linear frequency modulated (LFM) signals using the fractional Fourier transform," *Ultrasonics, Ferroelectrics and Frequency Control, IEEE Transactions on*, vol. 57, no. 10, pp. 2324–2333, 2010.

[45] D. Y. Kim, J. C. Lee, S. J. Kwon, and T. K. Song, "Ultrasound second harmonic imaging with a weighted chirp signal," in *IEEE Ultrasonics Symposium*, 2001, pp. 1477–1480.

[46] S. Harput, M. Arif, J. McLaughlan, D. M. J. Cowell, and S. Freear, "The effect of amplitude modulation on subharmonic imaging with chirp excitation," *Ultrasonics, Ferroelectrics and Frequency Control, IEEE Transactions on*, vol. 60, no. 12, pp. 2532–2544, 2013.

[47] U.S. Food and Drug Administration, "Information for manufacturers seeking marketing clearance of diagnostic ultrasound systems and transducers," FDA, Tech. Rep., 09-09-2008.

[48] J. G. Abbott, "Rationale and derivation of mi and ti - a review," *Ultrasound in Medicine & Biology*, vol. 25, no. 3, pp. 431–441, 1999.

[49] J. R. Sanchez and M. L. Oelze, "An ultrasonic imaging speckle-suppression and contrast-enhancement technique by means of frequency compounding and coded excitation," *Ultrasonics, Ferroelectrics and Frequency Control, IEEE Transactions on*, vol. 56, no. 7, pp. 1327–1339, 2009.

[50] J. Mamou, J. Ketterling, and R. Silverman, "Chirp-coded excitation imaging with a high-frequency ultrasound annular array," *Ultrasonics, Ferroelectrics and Frequency Control, IEEE Transactions on*, vol. 55, no. 2, pp. 508–513, 2008.

[51] J. Mamou, O. Aristizábal, R. H. Silverman, J. A. Ketterling, and D. H. Turnbull, "High-frequency chirp ultrasound imaging with an annular array for ophthalmologic and small-animal imaging," *Ultrasound in Medicine & Biology*, vol. 35, no. 7, pp. 1198–1208, 2009.

[52] S. Harput, J. McLaughlan, P. R. Smith, D. M. J. Cowell, S. D. Evans, and S. Freear, "Separating the second harmonic response of tissue and microbubbles using bispectral analysis," in *IEEE Ultrasonics Symposium*, 2012, pp. 1930–1933.

[53] G. Gurun, P. Hasler, and F. Degertekin, "Front-end receiver electronics for high-frequency monolithic cmut-on-cmos imaging arrays," *Ultrasonics, Ferroelectrics and Frequency Control, IEEE Transactions on*, vol. 58, no. 8, pp. 1658–1668, 2011.

[54] R. Guldiken, M. Balantekin, J. Zahorian, and F. Degertekin, "Characterization of dual-electrode cmuts: demonstration of improved receive performance and pulse echo operation with dynamic membrane shaping," *Ultrasonics, Ferroelectrics and Frequency Control, IEEE Transactions on*, vol. 55, no. 10, pp. 2336–2344, 2008.